It Takes Two: Bimodal interactions between the SARS-CoV-1 fusion peptide and Ca^{2+} ions promote membrane insertion and viral entry

Juliana Debrito Carten [1±], Miya K. Bidon [1±], George Khelashvili [4,5±], Marco R. Straus [2], Tiffany Tang [1], Javier A. Jaimes [2], Harel A. Weinstein [4,5*], Gary R. Whittaker [2,3*], and Susan Daniel [1*]

[1] Robert Frederick Smith School of Chemical and Biomolecular Engineering, Cornell University, Ithaca, NY, USA

[2] Departments of Microbiology & Immunology and [3] Public & Ecosystem Health, Cornell University, Ithaca, NY, USA

[4] Department of Physiology & Biophysics, Weill Cornell Medicine, New York, NY, USA

[5] Institute for Computational Biomedicine, Weill Cornell Medicine, New York, NY 10065, USA

*Corresponding authors:

Susan Daniel: sd386@cornell.edu

Gary Whittaker: grw7@cornell.edu

Harel Weinstein: haw2002@med.cornell.edu

[±] These authors contributed equally.

Abstract

In coronaviruses, the fusion peptide (FP) is situated within the membrane fusion domain of the spike protein, becoming exposed following proteolytic cleavages at the S1/S2 and S2' sites. After receptor binding-induced conformational changes, the FP penetrates the host cell membrane and mediates membrane fusion. Previous work has revealed the importance of calcium for SARS-CoV-1 FP structural stability and host membrane insertion. In this follow-up study, we systematically introduced charge-neutralizing alanine mutations in the negatively charged amino acids within the SARS-CoV-1 fusion peptide (E801A, D802A, D812A, E821A, D825A, D830A) to identify residues that likely bind to calcium. We assayed fusion competency by performing a syncytia-formation assay in VeroE6 cells and infectivity using pseudoparticles. The loss of single negatively charged residues D812 or D830 greatly reduced syncytia formation and produced noninfectious pseudoparticles. Furthermore, we observed a calcium-dependent decrease in the infectivity of the D825A and D830A pseudoparticles, as well as fewer syncytia in the cells expressing E821A/D825A double mutant FP. To clarify which residue pairs in the FP are most likely to bind calcium and promote host membrane insertion, we carried out molecular dynamics (MD) simulations of the various FP constructs. From our modeling, residue E801 is predicted to pair with either D830 or D802 to coordinate one calcium; a second calcium ion likely pairs residue E821 with either D812 or D825. We propose a model of bimodal calcium binding in the FP1 and FP2 domains, which anchors the SARS-CoV-1 FP in the host cell membrane to promote membrane insertion and fusion.

42 **Introduction**

43 Coronaviruses (CoVs) are a diverse family of enveloped single-stranded RNA viruses
44 responsible for causing respiratory and enteric diseases across a wide range of species (1, 2).
45 Three human coronaviruses have posed significant public health threats during the early 21st
46 century: the severe acute respiratory syndrome coronavirus (SARS-CoV-1) in 2002, (3), Middle
47 East respiratory syndrome coronavirus (MERS-CoV) in 2012 (4), and currently SARS-CoV-2 (5, 6).
48 SARS-CoV-2 vaccines have proven to be highly effective at preventing morbidity and death
49 during the pandemic; however, current experience demonstrates that there is an ever-present
50 need for antivirals as a parallel line of defense. Development of such therapeutics requires a
51 better understanding of the fundamental biology of coronaviruses and the intrinsic and
52 extrinsic determinants of viral entry.

53 In coronaviruses, viral entry is mediated by the highly conserved and complex spike (S)
54 glycoproteins, which form homotrimers in the virion membrane and interact with host cell
55 receptors, such as angiotensin-converting enzyme 2 (ACE2) and DPP4 (7). Upon spike-mediated
56 interaction with the host cell surface receptor, CoVs are proposed to utilize two different entry
57 pathways: an “early” route involving proteolytic priming at the cell surface and a “late” route
58 that follows the canonical endosomal/lysosomal pathways (8). The entry pathway utilized is
59 largely dependent on the local protease environment (9, 10). Previous work has shown that
60 SARS-CoV-1 can enter host cells via the early pathway when the transmembrane serine
61 protease 2 (TMPRSS2) and the virus receptor ACE2 are both present in the plasma membrane,
62 or when activated by exogenous trypsin after binding to the cell surface (11). SARS-CoV-1 can
63 also enter cells via the endosomal route where low pH-dependent proteases, such as cathepsin

64 L, cleave and prime the FP for membrane insertion and fusion. This latter pathway is likely the
65 predominant one used by SARS-CoV-1 in most laboratory cell lines (*e.g.* Vero cells)(9, 10, 12).
66 The entry flexibility seen across coronaviruses arises from the differential requirements
67 needed for protease priming and activation of the S protein. At the boundary between the S1
68 and S2 domains is the S1/S2 cleavage site, which is cleaved at position R667 by trypsin-like
69 proteases in SARS-CoV-1 (13), with an additional downstream cathepsin site present at T678
70 (14). This structurally exposed cleavage loop, common across the sarbecoviruses, separates the
71 S1 receptor-binding domain from the S2 fusion machinery of the spike protein (15). In SARS-
72 CoV-1, as with other CoVs, an additional S2' prime site (R797) is located N-terminally adjacent
73 to the fusion peptide (FP), which becomes liberated to facilitate membrane fusion following
74 cleavage (16). S2' cleavage allows the S2 domain to undergo a large conformational change
75 that favorably positions the FP for insertion into the host cell membrane (12). Given the
76 importance of the FP in initiating membrane fusion, it is not surprising to find significant
77 conservation of the amino acid sequence in this region of the S protein across many CoVs (17,
78 18). A second fusion active domain was also identified in SARS-CoV-1 downstream of S2 (16),
79 with the two domains subsequently considered to act together as part of an extended fusion
80 platform, FP1/FP2 (17).
81 Our previous work has focused on elucidating how calcium ions impact the structure
82 and function of the FP (FP1/FP2) during coronavirus entry. We have previously shown that for
83 SARS-CoV-1 and also for MERS-CoV, intra-and extracellular depletion of calcium leads to a
84 significant drop in pseudoparticle infectivity, with SARS-CoV-1 pseudoparticles showing a
85 greater reduction in infectivity than for MERS-CoV (17, 19). In addition, we have shown using

86 electron spin resonance (ESR) that the FPs of these viruses induce membrane ordering in a
87 calcium-dependent manner. We have further predicted the stoichiometry between the FP and
88 calcium ions to be 1:2 for SARS-CoV-1 and 1:1 for MERS-CoV using isothermal calorimetry (ITC)
89 (19), and observed that the SARS-CoV-1 FP adopts a conformation with a higher degree of α-
90 helicity in the presence of calcium and synthetic membranes (17, 19). Taken together, these
91 results indicate that direct interaction between calcium and the SARS-CoV-1 FP facilitates host
92 membrane insertion and fusion required for host cell entry.

93 The CoV FP sequence contains several highly conserved negatively charged amino acids
94 that flank the hydrophobic residues LLF that are known to interact with the host membrane
95 upon FP insertion (17). We and others have posited that like the SARS-CoV-2 FP (20), the SARS-
96 CoV-1 FP binds calcium at the conserved negatively-charged residues, which stabilize the local
97 structure of the FP and position it for optimal membrane penetration(17, 19); however, a
98 detailed mechanistic understanding of how these residues act together to facilitate membrane
99 insertion has remained unclear. Here, we build off of earlier mutagenic (18) and biophysical
100 characterizations (21) of the SARS-CoV FP which show that the negatively charged residues of
101 the SARS-CoV-FP (E801, D802, D812, E821A, D825, and D830) interact with calcium and are
102 important for infectivity to varying degrees. We present specific mechanistic insight regarding
103 the preferences and conformational consequences of the binding gathered from a combination
104 of mutagenesis studies and computational simulations. We first systematically examined the
105 effects of mutating charged residues in the SARS-CoV-1 FP on syncytia formation and viral
106 infectivity in the presence or absence of calcium to identify residues that likely interact with
107 calcium. We then used corresponding molecular dynamics simulations of the system to

108 determine which pairs of residues likely work together to mediate calcium binding. From these
109 simulations we have identified the FP residue pairs predicted to bind to calcium and position
110 the FP favorably for host membrane insertion.

111 Results

112 Generation and characterization of SARS-CoV-1 Spike fusion peptide mutants

113 Various structural conformations of the SARS-CoV-1 spike monomer have been solved using
114 Cryo-EM (PDB: 5XLR, 5WRG, 5X58) (22). From these pre-fusion structures, it is apparent that
115 the fusion peptide segment containing the core hydrophobic residues LLF adopts an α-helical
116 conformation, followed by a proximal disordered loop known to participate in cysteine-
117 mediated intramolecular disulfide bonding **(Fig 1).**

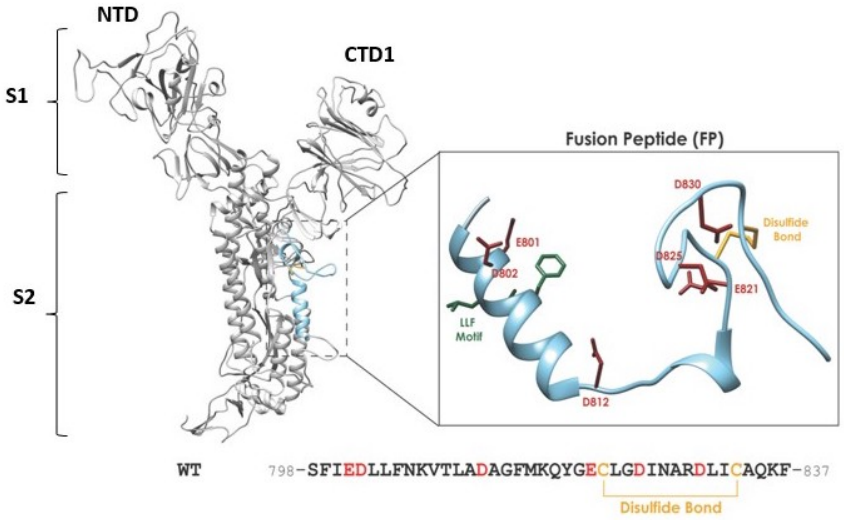

118

Figure 1. Structure of the SARS-CoV-1 Spike protein. The monomeric SARS-CoV-1 spike glycoprotein in the prefusion conformation (Gui et al. 2017; PDB: 5XLR). The β strand rich S1 subunit of the spike protein contains the C-terminal domain 1 (CTD1), which mediates ACE2 binding, and the N-terminal domain (NTD). The S2 subdomain contains mostly of α-helices and is comprised of two heptad repeat regions (HR1 and HR2) and the fusion peptide (FP). The fusion peptide is highlighted in light blue and expanded to show its predicted structure and the residues of interest in this study. The hydrophobic LLF residues appear in green, negatively charged residues in red, and the disulfide bond in yellow. Beneath the structure is the 40-amino acid long sequence of the WT FP (GenBank accession no. AAT74874.1). The single charge-to-alanine mutations generated in the aspartic (D) and glutamic (E) acids are indicated in red. The two cysteine residues that form a disulfide bond within the FP2 region are highlighted in yellow.

119

120

121 To determine the roles of the negatively charged residues found in the SARS-CoV-1 FP and their

122 involvement in calcium binding, we performed alanine substitutions of the six negatively

123 residues that are highly conserved across SARS-CoV-1, MERS-CoV, and SARS-CoV-2 **(Figs 1 and**

124 **2)**.

125

Figure 2. Generation of the single charge-to-alanine mutations in the SARS-CoV fusion peptide. (**A**) Alignment of the amino acid sequences of SARS-CoV, MERS-CoV, and SARS-CoV-2 FPs showing the highly conserved LLF motif (green), the negatively charged residues (red), and the intramolecular disulfide bond. (**B**) The sequences of the wild-type (WT) SARS CoV fusion peptide (GenBank accession no. AAT74874.1) and various mutants, containing the single charge-to-alanine mutations generated in the aspartic (D) and glutamic (E) acids. Charged residues appear in red and substitutions appear in green. Cysteine residues that form a disulfide bond appear in yellow.

126

127 We first made single amino acid (aa) substitutions (E801A, D802A, D812A, E821A, D825A,

128 D830A) in the wild-type SARS-CoV-1 FP. The wildtype and mutant forms of the SARS-CoV-1 S

129 gene were then cloned into pcDNA3.1 expression vectors to facilitate their transient expression

130 and characterization. To verify the expression of folded and active protein we assessed the

131 ability of the S to be appropriately cleaved for fusion activation. To achieve this, TPCK-trypsin

132 (1mg/mL) was added to cells 24 hours after transfection and the S proteins were isolated by

133 cell-surface biotinylation. Biotinylated proteins were retrieved following cell lysis using

134 streptavidin beads, resolved by gel electrophoresis, and immunoblotted for using a SARS-CoV-1

135 S polyclonal antibody (**Fig 3**).

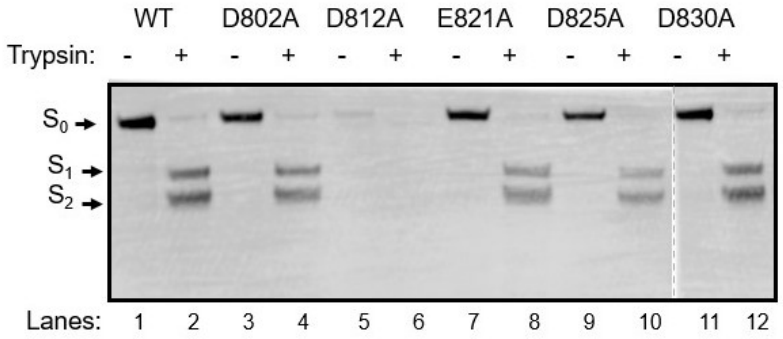

136

Figure 3. Cell surface biotinylation assay of SARS-CoV wild-type and single charge-to-alanine spike mutants. Spike immunoblot analysis of biotinylated WT and mutant S proteins transiently expressed in HEK293T cells, then left untreated (-) or treated (+) with 1 mg/mL Trypsin for 10 minutes. S_0 indicates the full-length, uncleaved spike protein. S_1 and S_2 note the S1 and S2 cleaved subunits of spike. Spike immunoblot showing the cell surface accumulation of WT S and the single charge-to-alanine mutants. Dotted lines indicate where lanes were re-ordered on the same immunoblot; n = 3 biological replicates

137

138 The resulting spike immunoblots displayed the full-length uncleaved S species (S_0) migrating at

139 ~185kDa in all untreated samples (**Fig 3, even lanes**). SARS-CoV-1 S mutants containing the

140 single mutations D802A, E821A, D825A, and D830A had comparable cell surface levels of S

141 protein to the wild-type protein, indicating that these mutants are not impaired in their

142 synthesis or trafficking to the plasma membrane. Significantly lower cell surface levels of the

143 D812A mutant were retrieved in comparison to WT spike (**Fig 3, lanes 5 and 6**); however,

144 comparable levels of the cleaved S1 and S2 subunits were observed occasionally following

145 TPCK-Trypsin treatment, indicating variability in the production or retrieval of this mutant in

146 this assay (**SI Fig 1B, lane 6**). Additionally, proteolytic cleavage of the D802A, D812A, E821A,

147 D825A, and D830A mutants occurred following treatment with TPCK-trypsin, indicating that

148 these mutants each had an accessible trypsin cleavage site and were able to be primed for

149 downstream fusion evens. The two lower molecular weight bands that appear at ~100kDa and
150 ~80kDa in the all TPCK-trypsin treated lanes are likely the S_1 and S_2 subunits, respectively (**Fig**
151 **3A and B**). These subunits have been detected previously following cleavage of a recombinant S
152 protein monomer by Trypsin at the S1/S2 cleavage site.

153 It should be noted that we were unable to detect surface levels of the E801A mutant on
154 the spike immunoblots (**SI Fig S2**). To further probe the nature of this residue's importance for S
155 protein stability, we substituted in the larger, nonpolar methionine (E801M), a polar and
156 uncharged glutamine (E801Q), a positively charged lysine (E801K) or even the close mimetic
157 negatively charged aspartic acid (E801D). None of these mutations, including the charge
158 mimetic E801D, restored the cell surface levels of the S protein to that of wild-type, indicating
159 the specific requirement of glutamic acid in this region of the FP (**Fig S2**).

160

161 **Analysis of the SARS-CoV-1 FP single point mutants' ability to promote syncytia formation**

162 Functional tests of the ability of S mutants to induce cell-cell fusion were performed
163 using a syncytia assay. WT or mutated S constructs were transiently expressed in VeroE6 cells, a
164 kidney epithelial cell line that expresses the ACE2 receptor (23). 24 hours following
165 transfection, cell-cell fusion was induced by treating cells with TPCK-Trypsin (2mg/mL) to cleave
166 the FP at the S1/S2 site. Syncytia were visualized by immunofluorescence using a SARS-CoV-1 S
167 antibody and cells were co-stained with DAPI to identify multinucleated cells. Syncytia were
168 quantified by counting every group of fused cells with a minimum of 4 nuclei and expressed as a
169 percentage of the total number of generic fluorescent particles counted in a field of view
170 (yes/no binary binning method). VeroE6 cells expressing the WT S readily formed syncytia with

171 an average of ~47.7% of fluorescent regions of interest (ROIs) being classified as syncytia (**Fig**

172 **4A and B**).

173

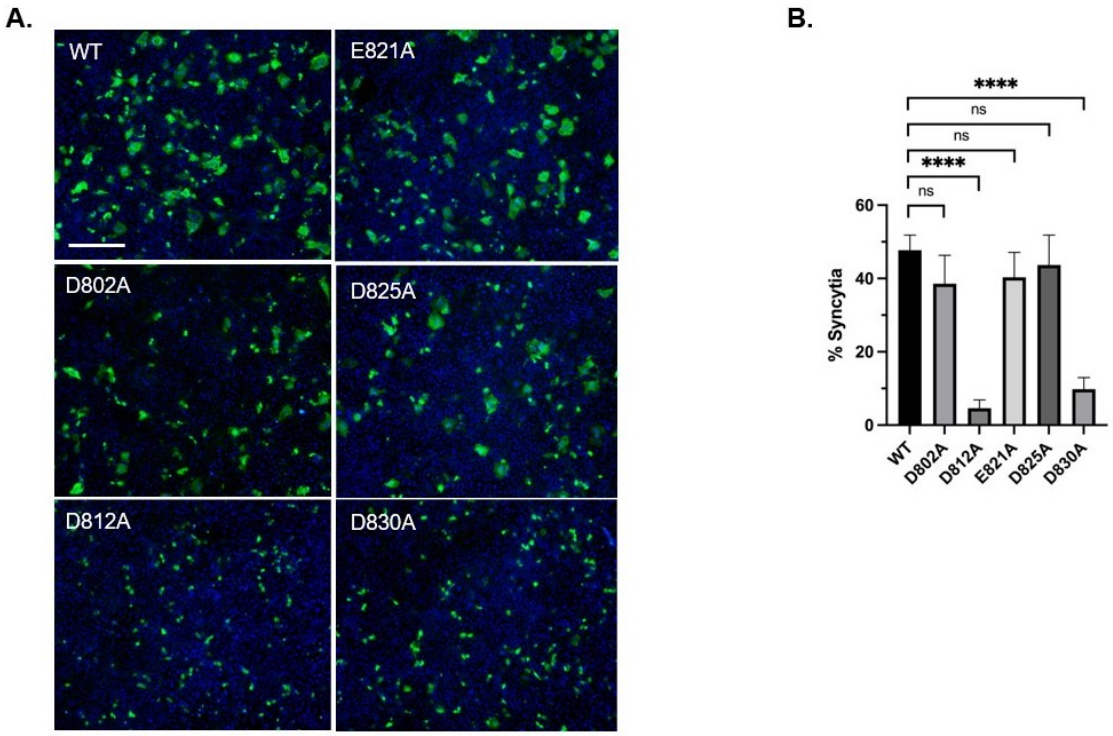

174

Figure 4. Syncytia formation in SARS-CoV wild-type and single charge-to-alanine mutant S-expressing VeroE6 cells. (**A**) Representative immunofluorescence images of VeroE6 cells expressing WT or single charge-to-alanine mutant S constructs. 24 h following transfection, cells were treated with 2mg/mL TPCK-trypsin for 5 minutes to cleave S proteins and induce syncytia formation. Cells were fixed and syncytia were visualized using a SARS-CoV S antibody (*green*). Nuclei were stained with DAPI and appear in blue. Images were taken at 10X magnification. Scale bars = 90 µm (**B**) Quantification of syncytia across each condition. **** denotes significance of $p < 0.0001$. n = a minimum of 3 biological replicates.

175

176 Similarly, VeroE6 cells expressing the D802A, E821A, or D825A mutants all exhibited

177 comparable syncytia formation to cells expressing WT S, indicating that loss of a negative

178 charge in these individual residues does not affect FP function in this assay (**Fig 4A and B**).

179 Conversely, cells expressing the D812A and D830A S mutants largely failed to form syncytia,

180 indicating the importance of these residues in FP mediated cell-cell fusion **(Fig 4A and B)**.

181 **Analysis of the SARS-CoV-1 FP single mutants' effect on viral infectivity**

182 We next tested the ability of the SARS-CoV-1 single mutants to infect cells using SARS-CoV-1
183 pseudoparticles as a surrogate for infectious virus. SARS-CoV-1 is designated a Risk Group 3
184 Select Agent that requires a specialized biosafety level 3 facilities for experimentation.
185 Pseudoparticles offer a safe alternative to live SARS-CoV-1 virus and enables experiments to be
186 carried out in BSL-2 level conditions (24). To generate SARS-CoV-1 pseudoparticles in HEK293T
187 cells, we used a three-plasmid co-transfection system with plasmids encoding: (1) the full
188 length CoV-1 surface S protein, (2) the murine leukemia virus (MLV) core proteins *gag* and *pol*,
189 or (3) a firefly luciferase reporter gene containing the MLV-MJ RNA packaging signal and flanked
190 by long terminal repeat (LTR) sequences (24). Upon successful particle fusion with the host cell
191 membrane, the luciferase reporter RNA transcript is reverse transcribed and expressed,
192 enabling a measurable readout of pseudoparticle entry. Our previous studies have shown that
193 this approach works well for assessing the infectivity of MERS-CoV (25), SARS-CoV-1 (17, 24),
194 and SARS-CoV-2 (26) pseudoparticles.
195 Incorporation of the WT and mutant S proteins into the SARS-CoV-1 pseudoparticles was
196 assessed using S immunoblotting (**Fig. 5A**). Pseudoparticles with WT or the mutant S proteins
197 D802A, D812A, E821A, D825A, and D830A show comparable levels of S protein incorporation
198 (**Fig 5A**). We believe that the observed higher molecular weight species on the S immunoblots
199 represents unresolved, detergent resistant S trimers present in the pseudoparticles (**Fig 5A**).
200 The slightly lower molecular weight band at ~185 kDa (S_0) represents full-length monomeric S
201 protein. The smallest band appearing at ~80kDa represents the S2 subunit (S_2). As expected,
202 we did not detect the E801A mutant in the SARS-CoV-1 pseudoparticles, likely due to its low
203 cellular expression or synthesis. After confirming the incorporation of the spike proteins into

204 the SARS-CoV-1 pseudoparticles, we tested their infectivity. Exposure of VeroE6 cells to WT

205 SARS-CoV-1 pseudoparticles results in a robust luminescent signal 72 hours post infection,

206 indicating successful viral entry and infection (**Fig 5B**).

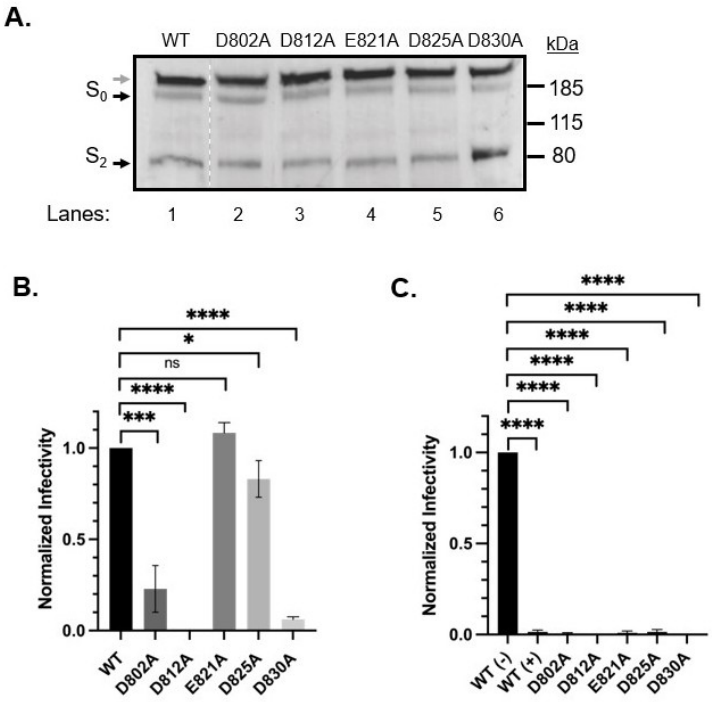

207

Figure 5. Infectivity of wild-type and single mutant SARS-CoV spike-containing pseudoparticles. (**A**) Spike immunoblot of pseudoparticles containing wild-type or single charge-to-alanine spike mutants. S_0 indicates the full-length, uncleaved spike protein. S_2 indicates the cleaved S2 subunit of spike. The prominent band above 185 kDa is likely higher order species of spike multimers (gray arrow). (**B & C**) WT and mutant SARS-CoV pseudoparticle infectivity assays in VeroE6 cells left untreated (B) or treated with 50 μM BAPTA-AM (C). *,*** and **** denote significance of $p < 0.05$, 0.001, or 0.0001, respectively. n = 3 biological replicates.

208

209 After confirming the incorporation of the spike proteins into the SARS-CoV-1

210 pseudoparticles, we tested their infectivity. Exposure of VeroE6 cells to WT SARS-CoV-1

211 pseudoparticles results in a robust luminescent signal 72 hours post infection, indicating

212 successful viral entry and infection (**Fig 5B**). E821A-containing pseudoparticles did not exhibit a

213 significant change in infectivity compared to wild-type particles, suggesting this residue does

214 not have a major effect on FP function (**Fig 5B**). In contrast, the D802A, D812A, and D830A

215 mutant pseudoparticles all showed a pronounced decrease in infectivity, with the D812A and
216 D830A mutations resulting in essentially noninfectious particles. D825A-containing
217 pseudoparticles showed a slight but significant (20%) decrease in infectivity. These results
218 indicate that mutations in three highly conserved negatively charged residues in the S protein's
219 FP (D802, D812, and D830) significantly decrease SARS-CoV-1 pseudoparticle infectivity.

220 We then examined the effect of depleting the extra- and intracellular calcium on
221 pseudoparticle infectivity by using the cell-permeable calcium chelator 1,2-bis(2-
222 aminophenoxy)ethane- *N,N,N'N'*- tetraacetic acid tetrakis (BAPTA-AM). We have previously
223 optimized the concentrations of BAPTA-AM so as not to significantly impact cell viability (17,
224 25). VeroE6 cells were treated with 50 µM BAPTA-AM briefly prior to and during pseudoparticle
225 infection, harvested, and assayed for luminescence (**Fig 5C**). Depletion of extra- and
226 intracellular calcium rendered the WT pseudoparticles noninfectious and similar results were
227 observed across all the single mutant pseudoparticles tested; none of the pseudoparticles were
228 infectious in the absence calcium. These data indicate that depletion of extra- and intracellular
229 calcium exerts a severe effect on pseudoparticle infectivity and is consistent with our previous
230 findings. Due to the differential effect observed on infectivity with individual mutations and the
231 loss of available calcium, we deduced that the FP uses multiple negatively charged residues to
232 bind to calcium ions. We hypothesized that mutating certain residues (E821A, D825A)
233 individually does not lead to a complete loss in pseudoparticle infectivity since other charged
234 residues in the FP can compensate by serving as alternate or primary calcium binders.

235

236 **Multiple negatively charged residues mediate SARS-CoV-1 fusion peptide's calcium binding**

237 The FP contains two defined regions: the N-terminal region starting just upstream from
238 the S2' cleavage site (aa798-819), termed FP1, and the downstream region that includes a
239 critical disulfide bond (aa820-837), termed FP2 (16, 18). Lai *et al.* reported a stoichiometry of
240 two calcium ions per single SARS-CoV-1 FP, therefore we reasoned that FP1 and FP2 regions
241 each contain residues that can coordinate calcium binding (17). In FP1, the alanine substitutions
242 of residues D802 and D812 rendered their pseudoparticles non-infectious, as did the D830A
243 substitution in FP2. To test the hypothesis that the SARS-CoV-1 FP utilizes multiple residues to
244 mediate calcium binding, we created double residue substitutions to generate the
245 E821A/D825A mutant. Neither residue when individually mutated affected syncytia formation
246 (**Fig 4B)**; however, the D825A mutant exhibited a mild reduction in infectivity (**Fig 5B**). We
247 hypothesized that these residues might serve as alternate calcium binding residues. Thus, we
248 predicted the E821A/D825A double mutant to have a greater effect on syncytia formation and
249 pseudoparticle infectivity. We also generated the E821A/D830A mutant as a negative control
250 because the D830A mutation is phenotypically dominant, blocking syncytia formation and
251 reducing pseudoparticle infectivity (**Fig 6A**).

252 As with the single charge-to-alanine S mutants, we transiently expressed the double
253 mutant constructs in HEK-293T cells and performed a biotinylation assay to determine if they
254 were synthesized, trafficked to the plasma membrane, and able to be cleaved by Trypsin (**Fig**
255 **6B**). The double mutants have comparable cell surface levels of full-length protein compared to
256 WT S, indicating that they are similarly expressed and trafficked to the plasma (**Fig 6B, odd**
257 **lanes**). In addition, the nearly complete disappearance of the full-length mutant S species

258 following trypsin treatment indicates that all mutants are cleaved by trypsin similar to WT S (**Fig**

259 **6B, even lanes)**.

260

261

262

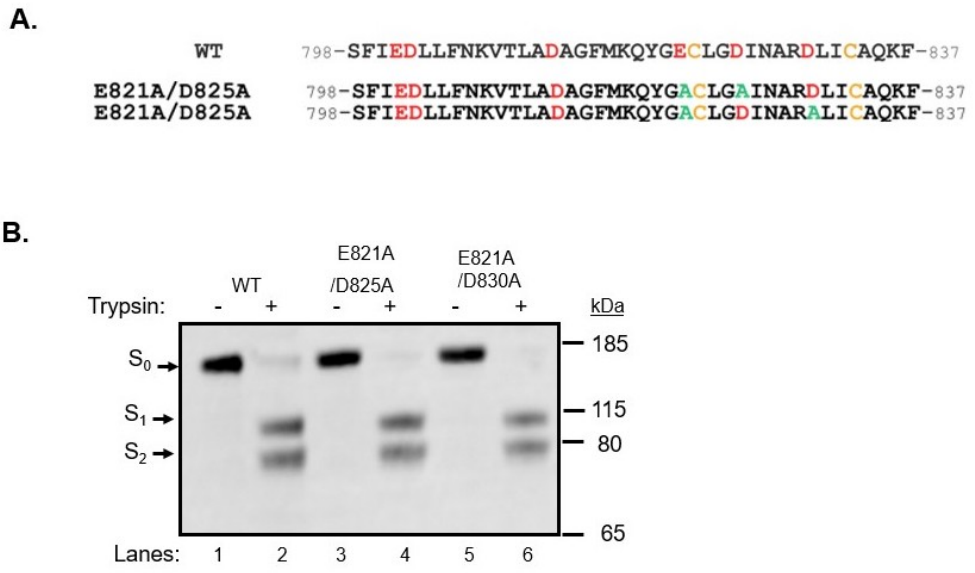

263

Figure 6. Generation and validation of double charge-to-alanine SARS-CoV spike mutants. (**A**) The sequence of the wild-type SARS fusion peptide, beneath which appear the double charge-to-alanine mutants, with mutated aspartic (D) and glutamic (E) acids. WT charged residues appear in red and substitutions appear in green. Yellow indicates the cysteine residues that form an intramolecular disulfide bond. (**B**) Cell surface biotinylation assay of SARS-CoV wild-type and mutant spike proteins generated transiently in HEK293T cells. Spike western blot analysis of biotinylated WT and mutant S proteins left untreated (-) or treated (+) with 1 mg/mL TPCK-trypsin for 10 minutes. S_0 indicates the full-length, uncleaved spike protein. S_1 and S_2 indicate the S1 and S2 cleaved subunits of spike; n = 3 biological

264 replicates.

265 We tested the functionality of these S mutants using the previously described syncytia

266 assay. VeroE6 cells transiently expressing the double mutant E821A/D830A displayed a

267 significant defect in syncytia formation (< 10% syncytia) in comparison to WT S-expressing cells

268 **(Fig 7A and B)**. Because the individual D830A mutant exhibited a severe defect in syncytia

269 formation, this phenotypic effect dominates the functional readout and we see no additional

270 effect on syncytia formation. The E821A/D825A double mutant exhibited a reduction in
271 syncytia formation (29.7% syncytia) in comparison to WT, indicating a potential additive effect
272 when the two individual mutations are combined.

273 We then generated pseudoparticles containing the E821A/D825A double mutant and
274 assayed the incorporation of the mutant spike into the pseudoparticles via spike
275 immunoblotting.

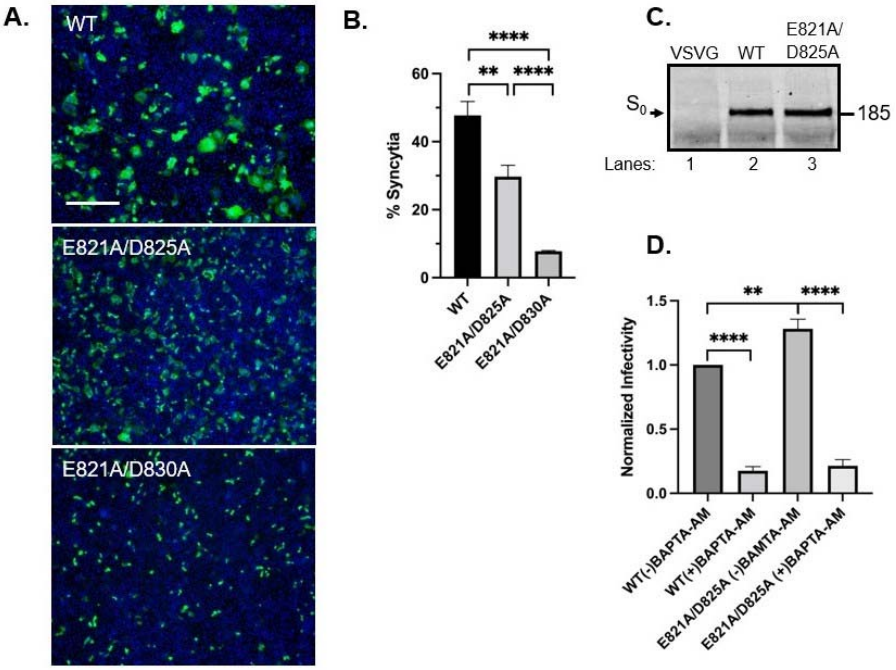

276

Figure 7. Assessment of syncytia formation ability and infectivity of SARS-CoV double mutant E821A/D825A. (**A**) Representative immunofluorescence images of VeroE6 cells expressing WT, E821A/D825A, or E821A/D825A constructs. The E821A/D825A construct served as a negative control. 24 h following transfection, cells were treated with 2mg/mL TPCK-trypsin for 5 minutes to cleave S proteins and induce syncytia formation. Syncytia were visualized using a SARS-CoV S antibody (*green*) following fixation. Nuclei were stained with DAPI and appear in blue. Images were taken at 10X magnification. Scale bars = 90μm (**B**) Quantification of syncytia across each condition.(**C**) Spike immunoblots of pseudoparticles containing VSVG (no spike control), WT, or mutant E821A/D825A spike. S_0 indicates the full-length, uncleaved spike protein. (**D**) WT and E821A/D825A SARS-CoV pseudoparticle infectivity in VeroE6 cells left untreated (-) or treated with 50 μM BAPTA-AM (+).** and **** denote significance of $p < 0.05$ and 0.0001, respectively. n = 3 biological replicates

277

278 The E821A/D825A mutant pseudoparticles exhibited similar S protein levels to the WT
279 pseudoparticles (**Fig 7C**). Interestingly, VeroE6 cells infected with the mutant E821A/D825A
280 pseudoparticles exhibited a 28% increase in infectivity compared to WT pseudoparticle infected
281 cells (**Fig 7D**). As was previously demonstrated, depletion of extra- and intracellular calcium via
282 BAPTA-AM treatment causes a severe loss of infectivity for both WT and mutant E821A/D825A
283 pseudoparticles **(Fig 7D).**
284
285 **Molecular Dynamics simulations identify the modes of the SARS-CoV-1 FP's calcium binding**
286 The effects on cell-cell fusion and infectivity exhibited by the D802A, D812A and D830A
287 mutants, as well as the calcium-dependent loss of infectivity in the E821 and D825 mutants,
288 implied that the FP contains multiple sites of calcium binding required for viral entry. Our ability
289 to determine which residue pairs in the FP coordinate calcium binding was limited using our *in*
290 *vivo* mutagenesis approaches; therefore, we carried out atomistic molecular dynamics (MD)
291 simulations of the SARS-CoV-1 FP to predict the preferred modes of calcium binding and
292 membrane insertion. In particular, this MD approach allowed us to examine residue 801, which
293 was refractory to mutagenesis.
294 To monitor the spontaneous binding of calcium to the FP, we collected 18 independent MD
295 trajectories of 640ns in length for each construct. Following the analysis protocols described
296 recently for SARS-CoV-2 FP simulations (20, 27), the various modes of interactions between the
297 SARS-CoV-1 FP and calcium ions were assessed in the trajectories by monitoring: i) the
298 distances between the calcium ions in solution and the side chains of all acidic residues in the
299 peptide; and ii) the pairwise distances between the side chains of all acidic residues.

300 Summarized in **Fig S3** are the observed events of simultaneous association of two calcium ions
301 with various pairs of FP residues in the individual trajectories of the WT and the mutant systems
302 (see *red* and *blue* rectangles). The combined statistics for each construct (*i.e.,* the total number
303 of binding events for different pairs of residues) are summarized in **Fig 8**.

304 These results show the modes of calcium coordination in the WT protein, identifying the
305 most frequent modes involving residue pairs E821/D825 (5 out of 18); E801/D802 and
306 E801/D830 (4/18 each); and D812/E821 (2/18). Notably, a similar pattern of coordination
307 preference was observed in our recent computational studies of calcium association with SARS-
308 CoV-2 FP (20). Moreover, simultaneous binding of calcium ions to the SARS-CoV-2 FP residue
309 pairs equivalent to E801/D802 and D812/E821 produced the peptide conformations suitable for
310 membrane penetration. In contrast, conformations that stabilized calcium binding to residues
311 equivalent to the E821/D825 pair did not enable sustained bilayer insertion.

312

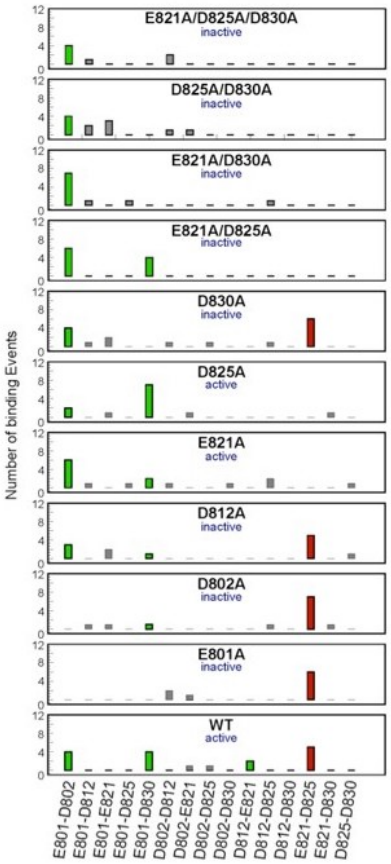

Figure 8. Predicted modes of Ca^{2+} and SARS-CoV fusion peptide binding. Number of Ca^{2+} binding events to different pairs of anionic residues in SARS-CoV FP in the simulations of the WT and the mutant constructs (labeled in each panel). The experimentally measured phenotypes for each construct are shown (active or inactive). The mode of Ca^{2+} ion association predicted to be inhibitory for membrane insertion (E821-D825) is shown in *red*, and the modes of Ca^{2+}association predicted to facilitate membrane insertion are depicted in *green*.

313

314 From these MD simulations of the SARS-CoV-1 FP constructs, we were able to predict the
315 phenotypes for each construct (active or inactive). The mode of calcium ion association
316 predicted to be inhibitory for membrane insertion (E821-D825) is shown in *red*, and the modes
317 of calcium association predicted to facilitate membrane insertion are depicted in *green* boxes
318 (**Fig 8**). In those constructs with single mutations that were predicted to not have fusion activity
319 (E801A, D802A, D812A, and D830A) we showed that only the calcium-coordination mode
320 involving the E821/D825 pair persists, but not the D812/E821 pair of residues (**Fig 8**).

321 Conversely, in the SARS-CoV-1 FP single mutants that maintained WT-like fusion activity (E821A
322 and D825A), we did not observe the E821/D825 residues predicted to participate in calcium
323 binding. In these function-preserving mutants we identified additional modes of calcium
324 binding that are enhanced in comparison to the WT system: E801/D802 in mutant E821A, or
325 E801/D830 in mutant D825A. For the SARS-CoV-1 FP constructs with multiple mutations, our
326 MD trajectories revealed an overall reduced calcium binding ability (**Fig 8** and **Fig S4**).
327

328 **SARS-CoV-1 FP propensity for membrane insertion is regulated by modes of calcium binding**

329 Overall, the above computational results reveal that the calcium binding patterns of SARS-
330 CoV-1 FP are very similar to those of SARS-CoV-2 FP (20). On this basis, membrane insertion of
331 the SARS-CoV-1 FP could be expected to be enhanced by the modes of calcium binding
332 involving the E801/D802 and D812/E821 pairs of residues, and to be reduced by the ones
333 involving the E821/D825 pair. To test this premise, we carried out MD simulations of two
334 models of the WT SARS-CoV-1 FP spontaneously associating with the lipid membrane (see
335 **Methods**). In one, the peptide was interacting with 2 calcium ions at the E801/D802 and
336 D812/E821 sites (Model 1), and in the second, 2 calcium ions were bound to the E801/D802
337 and E821/D825 pairs (Model 2). Each structure was simulated in 36 independent replicates,
338 each run for ~0.9-1.0 µs (see **Methods**).

339 Analysis of these trajectories revealed that, indeed, Model 1 extensively penetrated the
340 membrane, while the membrane insertion of the Model 2 was negligible. This can be seen from
341 the plots presented in **Fig 9** comparing frequencies of membrane insertion for each SARS-CoV-1
342 FP residue in the simulations of Model 1 and Model 2 structures.

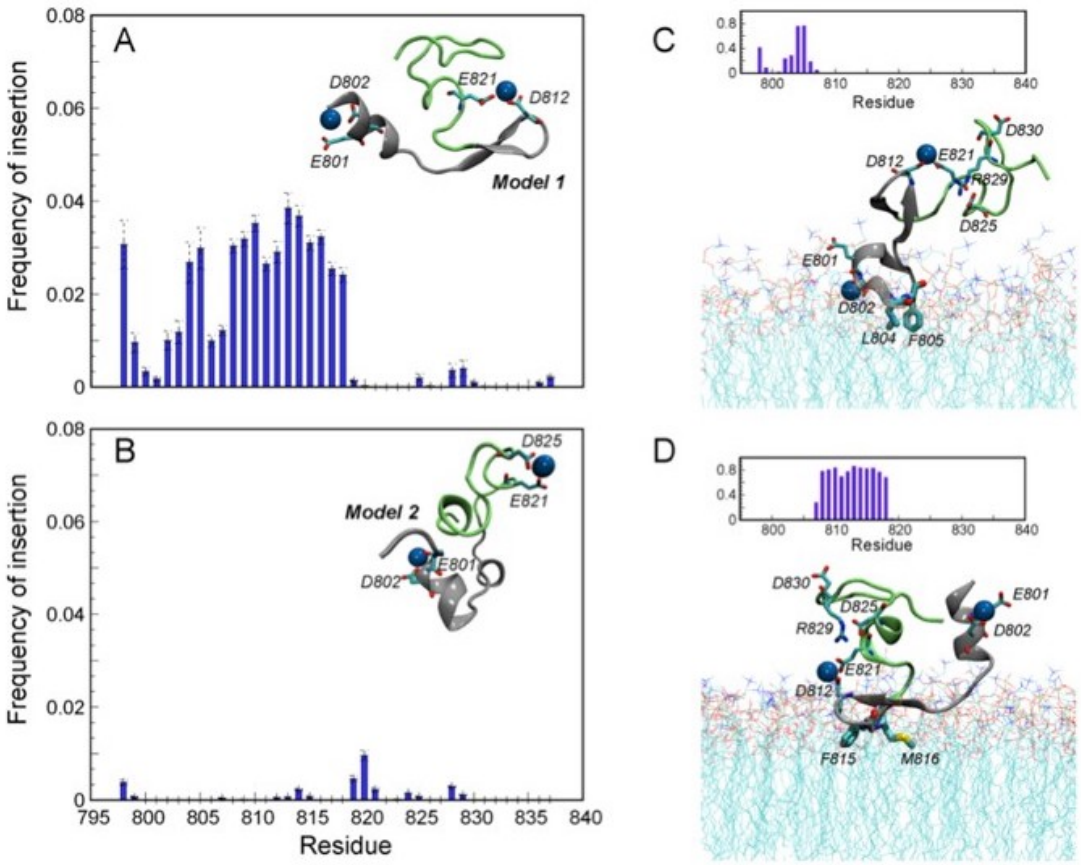

Figure 9. Membrane insertion for FP1 and FP2 domains of SARS-CoV fusion peptide. (**A-B**) Frequency of membrane insertion for each residue of SARS-CoV FP in the MD simulations of Model 1 (**A**) and Model 2 (**B**) constructs, which differ in the mode of Ca^{2+} coordination (see text). The ribbon diagrams in the panels show the corresponding structures. Ca^{2+} coordinating anionic residues are indicated in black text; Ca^{2+} ions are shown as blue spheres. The FP1 and FP2 parts of the fusion peptide are colored in silver and green, respectively. (**C-D**) The same frequency calculations but done separately for two representative trajectories in Model 1 set in which the observed membrane insertions involved the N-terminal LLF motif (**C**) and the more centrally located (F815-M816) hydrophobic segment (**D**). The corresponding ribbon diagrams illustrate the structural features of these two distinct insertion modes highlighting (in black) positions of the anionic residues, the hydrophobic residues penetrating the membrane, and the R829 residue interacting with D825. The same color code applies here as in panels A-B.

The membrane insertion was quantified by monitoring the z-coordinate of the C_α atom of each residue in the peptide. A residue was considered inserted into the membrane if the z-distance between its C_α atom and the second carbon atom in the tail of a POPC lipid (atom C22 in CHARMM36 notation) was <5Å. In Model 1 (**Fig 9A**), the N-terminal FP1 segment of the fusion peptide shows strong propensity for bilayer insertion, while in Model 2 the insertion is minimal (**Fig 9B**).

351

352 The detailed analysis of the individual trajectories in the Model 1 set revealed two distinct
353 modes of bilayer penetration for SARS-CoV-1 FP, similar to our findings for the SARS-CoV-1-2
354 FP. Thus, the Model 1 construct penetrates the bilayer either with its N-terminal LLF motif (**Fig**
355 **9C**) or with the more centrally located hydrophobic F815-M816 segment (**Fig 9D**). Interestingly,
356 the two insertion modes appear to alternate which calcium ion is neighboring the inserted
357 portion. Indeed, when the LLF is inserted, the calcium ion associated with the neighboring
358 E801/D802 residues is bound to the membrane while the other calcium binding site
359 (D812/E821) is situated away from the membrane surface (**Fig 9C**). In the case of the F815-
360 M816 insertion, the position of the calcium binding loci with respect to the membrane is
361 reversed – the one associated with the D812/E821 pair is membrane-bound, while the
362 E801/D802 pair is located farther from the bilayer (**Fig 9D**). We also note that in both cases, the
363 remaining anionic residues in the peptide (*i.e.* the ones not engaged with the calcium ions) are
364 either solvent exposed (D830) or engaged with electro-neutralizing interactions with
365 neighboring basic residues (D825/R829) (**Fig 9C and D**). These results support a mechanistic
366 model in which membrane penetration of the SARS-CoV-1 FP is significant only for specific
367 modes of calcium binding to the peptide, i.e., to the E801/D802 and D812/E821 pairs of
368 conserved acidic residues. Moreover, calcium binding at the E821/D825 pair is predicted to
369 inhibit membrane insertion.

370

371 **Discussion**

372 Previous work done on the SARS-CoV-1 FP has implicated all of the negatively charged
373 residues as calcium binders, but to varying degrees. Early structure-function work on the SARS-
374 CoV-1 FP showed the importance of general FP regions first, with the residues flanked by
375 cysteines (C822-C833) identified as important for membrane fusion activity (18). FP residues
376 that when mutated caused pronounced effects on syncytia formation and pseudoparticle
377 infectivity were then identified (D812 and D830), but before the importance of calcium during
378 viral entry was known (16). Recent biophysical characterizations of the FP found that mutation
379 of residue D812 in the FP1 region has the greatest effect on membrane ordering, calcium-
380 specific FP binding, and calcium-induced FP structural changes. Residue D830 in the FP2 region
381 (labeled 831 in their manuscript) was also found to be important, causing of loss of membrane
382 ordering and calcium sensitivity when mutated. In this study, we have taken a two-pronged
383 approach to identify how the negatively charged residues in the SARS-CoV-1 FP likely bind to
384 calcium during viral entry: biological studies and molecular dynamics simulations. We first
385 carried out syncytia formation and infectivity assays with single charge-to alanine FP mutants
386 E801A, D802A, D812A, E821A, D825A, and D830A (**Fig 2**), confirming that all mutants were
387 synthesized, accumulated at the cell surface comparable to WT S, and were able to be cleaved
388 by Trypsin (**Fig 3**).

389 We next tested the fusion competency of the single FP mutants using a syncytia
390 formation assay. VeroE6 cells expressing the D802A, E821A, and D825A mutants all formed
391 syncytia similar to WT S expressing cells (**Fig 4**). Conversely, cells expressing the D812A or
392 D830A mutants exhibited a pronounced cell-cell fusion defect (**Fig 4**). Infectivity assays
393 performed with pseudoparticles largely produced the same results: infections with E821A and

394 D825A S-containing pseudoparticles resulted in luminescence levels comparable or minorly
395 reduced to WT-containing pseudoparticles. However, pseudoparticles containing the D802A,
396 D812A, or D830A mutations were unable to infect VeroE6 cells as well. These results indicate
397 that when calcium levels remain unchanged, loss of an individual negatively charged residue in
398 FP position D802, D812, or D830 is sufficient to cause a substantial decrease in infectivity. As
399 previously mentioned, mutagenic studies of the SARS-CoV-1 FP found that mutations in the
400 SARS-CoV-1 residues D812 (D812A) and D830 (D830L) led to a decrease in syncytia formation
401 and pseudotyped virion infectivity (16, 18). Taken together, these data suggest that these
402 residues are essential in a non-redundant manner to the function of the SARS-CoV-1 fusion
403 peptide.

404 We then tested the requirement of intracellular calcium on pseudoparticle infectivity by
405 treating cells with a membrane permeable calcium chelator, BAPTA-AM, prior to pseudoparticle
406 infection. Following cell treatment with BAPTA-AM, WT and all mutant FP-containing
407 pseudoparticles are no longer infectious (**Fig 5C**). It is apparent from these data that this
408 approach could not assay specific FP residues' sensitivity to intracellular calcium. Disruption of
409 physiological concentrations of calcium is known to impact the fusion and infectivity of SARS-
410 CoV-1 and SARS-CoV-2 (28). We propose that calcium chelation via BAPTA-AM treatment
411 disrupted endosomal calcium concentrations causing a major reduction in endosomal fusion of
412 WT pseudoparticles, as SARS-CoV-1 enters VeroE6 cells primarily via the endosomal/lysosomal
413 pathway. BAPTA-AM treatment likely disrupted endosomal calcium levels which left
414 pseudoparticles unable to fuse with the endosomal/lysosomal membranes. We acknowledge
415 the potential impacts, both direct and indirect, that BAPTA-mediated depletion of calcium may

416 have on early pathway entry mechanisms. Calcium levels are proposed to affect host cell
417 receptor interactions at the plasma membrane; the SARS-CoV-2 spike protein's receptor
418 binding domain contains an RGD (Arginine-Glycine-Aspartate tripeptide) motif that is predicted
419 to bind to integrins in a calcium-dependent manner (29). ACE2 receptor turnover has also been
420 proposed to be a calcium-dependent process based on numerous lines of evidence
421 demonstrating the involvement of the calcium-binding protein, calmodulin (30-32). Because
422 calcium plays many important roles in cells and during viral infection, we believe that the loss in
423 infectivity we observed in our pseudoparticle assay reflects the cumulative effect of calcium
424 disruption on multiple pseudoparticle entry steps.

425 Previous mutagenic studies of the FP using biophysical readouts of function suggested
426 that FP residues display varying sensitivities to calcium, with the FP2 residues E821 and D825
427 showing modest calcium sensitivities and effects on function when mutated (21). We therefore
428 generated a double mutant (E821A/ E825A) to determine if these residues, when mutated
429 together, caused a more pronounced biological phenotype. We also generated the
430 E821A/D830A double mutant to serve as a negative control. Consistent with the single D830A
431 mutant, we observed a fusion defect in VeroE6 cells transiently expressing the E821A/D830A
432 mutant (**Fig 7A and B**). Furthermore, the E821A/E825A double mutant showed a significant
433 reduction in the percentage of syncytia formed, suggesting that the genetic effect is additive at
434 these loci (**Fig 7B**). When then assayed the infectivity of this mutant using pseudoparticles,
435 showing first that the double mutant E821A/D825A was successfully incorporated into
436 pseudoparticles (**Fig 7C**). In comparison to WT FP-containing pseudoparticles, the E821A/D825A
437 double mutant showed an increase in infectivity, while treatment with BAPTA-AM rendered

438 both types of pseudoparticles essentially noninfectious (**Fig 7D**). Although we cannot fully
439 reconcile why we observe a decrease in syncytia formation and an increase in infectivity for the
440 E821A/D825A-containing pseudoparticles, we hypothesize that these mutations may be
441 detrimental to spike-mediated fusion but advantageous at a downstream (post-fusion) event
442 which contributes favorably to viral replication.

443 From our *in vivo* findings, which confirmed the functional requirements of the
444 negatively charged residues in the FP, we then focused on identifying the residues that form a
445 calcium-binding platform. Because mutation of either FP residue D812 or D830 resulted in a
446 complete loss in S fusion competency and pseudoparticle infectivity, we predicted that they are
447 essential residues for calcium binding. In addition, residues E821 and D825 appeared to serve
448 as calcium binding alternates but did not appear to be supporting FP function in a major way.
449 These inferences were probed using molecular dynamics (MD) simulations of the calcium-
450 loaded SARS-CoV-1 peptide with the membrane. Exploring the probability of each FP residue
451 interacting with the membrane in the identified calcium-binding modes reveals the preferred
452 mode of peptide insertion to be with the N-terminal end interacting with a calcium ion
453 coordinated by residues E801 and D802 (**Figs 8 and 10**). The depth of insertion and the
454 determinant role of the calcium ion in facilitating membrane insertion are identical to the
455 findings for the SARS-CoV-2 peptide and are in agreement with the experimental
456 measurements of SARS-CoV-1 FP membrane insertion by Lai *et al* (17, 25, 33). That calcium
457 interacts with the same highly conserved, charged residues in the FPs of SARS-CoV-1 and SARS-
458 CoV-2 is not surprising.

459 Results from our computational modeling of SARS-CoV-1 FP-membrane interactions in the
460 presence of calcium show that the propensity of the SARS-CoV-1 FP for membrane insertion is
461 dictated by specific modes of calcium binding. The calcium binding mode that enables the most
462 sustained membrane penetration involves the initial association of the peptide with the bilayer
463 through a calcium binding site located near the N-terminus of the peptide. This site
464 (E801/D802) is made accessible following enzymatic cleavage and is inserted into the
465 membrane via the insertion of the juxtaposed hydrophobic segment (the LLF motif). In this
466 process, all anionic residues of the peptide are either engaged with calcium ions, with
467 neighboring basic residues, or remain solvent exposed away from the membrane. Based on the
468 preferred modes of calcium-loaded FP interaction with the membrane, we propose that the
469 binding of calcium following S protein cleavage at the S2' site creates an energetically feasible
470 membrane insertion process composed of the following steps: (1) steering of the peptide
471 towards the bilayer surface; (2) exposure of the hydrophobic layer of the membrane to the
472 conserved N-terminal LLF motif of the FP anchored by the calcium interactions with the
473 phospholipid headgroups; and (3) shielding of the anionic residues of the peptide by the
474 preferred inserting conformation of the FP to prevent their negative charge from interfering
475 with membrane insertion (**Figure 9**). These three components became evident from the
476 analysis of the MD simulation trajectories presented here for the SARS-CoV-1 FP and bear a
477 very high similarity to results from computational studies of the SARS-CoV-2 FP (20).

478 Remarkably, in both the SARS-CoV-2 FP simulations (34) and here, we observed a calcium
479 binding mode that inhibits long-lasting membrane insertion. In this mode calcium association
480 with the E821/D825 pair (corresponding to the D839/D843 in SARS-CoV-2 FP) positions the LLF

481 motif near the negatively charged D812 residue at the membrane surface (**Fig 9B**). This
482 eliminates the favorable effect of the negative charge screening by the calcium, so that the
483 peptide bilayer encounters are transient and do not lead to penetration by the LLF motif. This
484 mechanistic model, which highlights the role of the positioning of the D812 residue in specific
485 calcium binding modes, is supported by our findings for the SARS-CoV-1 S mutants, as it was
486 previously found to be an impactful mutation in the SARS-CoV-1 FP (16). A recent study from
487 Koppisetti *et al* asserts that a calcium ion may be binding to D843/D849 in SARS-CoV-2 FP
488 (corresponding to D825/D830 in SARS-CoV-1 FP); however, as shown from the simulations in
489 this study and Khelashvili *et al*, there is a high likelihood that the second calcium ion will bind to
490 D812/D821 (corresponding to the D830/D839 in SARS-CoV-2 FP) for the maximal membrane
491 penetration (20, 35). Recent NMR studies regarding the membrane interaction with the fusion
492 peptide still have yet to be fully resolved, as current models use bicelles (35) and micelles (36),
493 which do not completely capture the composition of the bilayer as was done for the
494 computational modeling shown here; though the model of membrane insertion proposed by
495 Koppisetti *et al (35)* most aligns with our proposed CoV FP interaction with bilayer (**Fig 9**).
496 Thus, as shown in **Figs 8** and **9** and summarized in **Fig 10**, mutations that create a high
497 propensity for the calcium binding mode involving the E821/D825 pair, stabilize peptide
498 conformations that are non-productive for membrane penetration and are found here to
499 inactivate the FP (**Fig 9**).
500
501
502

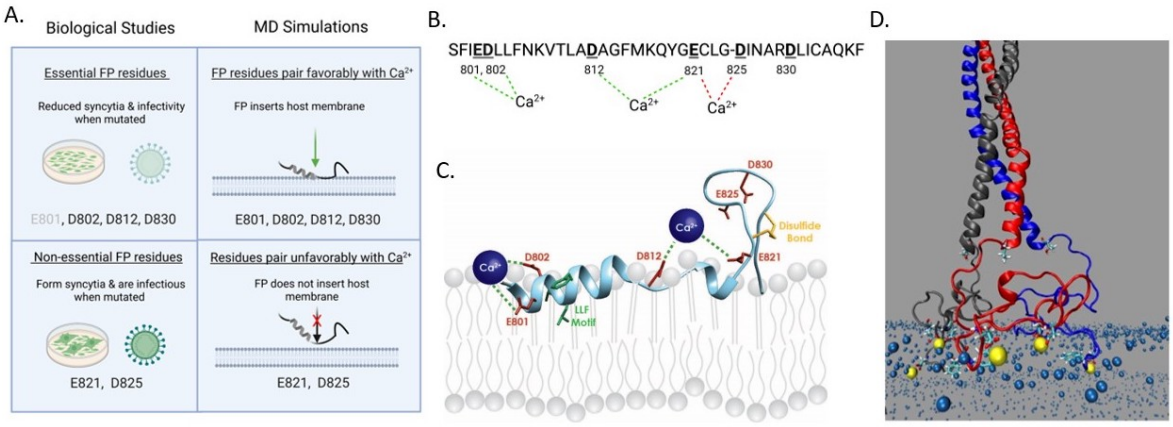

Figure 10. Summary of SARS-CoV-1 FP mutagenesis and MD simulations work. (A) The FP residues found to be necessary to promote cell-cell fusion and infectivity (biological studies) are the same residues predicted to pair with calcium to promote membrane insertion (MD simulations). The mutant E801A was not detected in our biological studies and appears in gray. (**B**) The FP residue pairings with calcium ions predicted to promote (green dashed lines) or inhibit (red dashed lines) membrane insertion. (**C**) A proposed model of the key charged residues in SARS-CoV-1 FP and their interactions with calcium ions and the membrane (outer leaflet). Depicted is the insertion of the FP1 subdomain, with the E801/D802-Ca^{2+} pairing predicted to promote membrane insertion of the LLF residues. D812 is predicted to bind Ca^{2+} with E821 to promote membrane interactions. The FP structure is based on the SARS-CoV-1 pre-fusion conformation (PDB: 5XLR). (**D**) A model of the SARS-CoV-1 trimer interacting with the calcium ions (in yellow, only 5 in view) and the host membrane. Upon interaction with calcium, the FP1 region adopts a more helical structure and can penetrate the host cell membrane to facilitate membrane fusion. BioRender was used to generate part of this figure.

Current studies on SARS-CoV-2 S protein classified the disordered portion of the FP in the FP2 domain as the FPPR (fusion peptide proximal region), which includes the charged residues D839/D843/D848 or E821/D825/D830 equivalent in SARS-CoV-1 FP (20, 37). This FPPR region was determined to be important, as it binds to the RBD through the CTD1, and maintains the closed pre-fusion S trimer(37). This is due to the tight packing around the disulfide bond reinforced by a bond between K835 and D848 (K817 and D830 in SARS-CoV-1 FP). The equivalent residue in SARS-CoV-1 FP, based on biological studies, is a critical residue (37). Mutating D830 removes the binding partner of K817, thereby loosening the 'knot' of the structured FPPR in maintaining the closed form of the trimeric S protein (37). Without the

515 reinforcements, we may lose the optimal structural conformation of the S protein upon
516 receptor binding to expose the S2' cleavage site to promote successful proteolytic cleavage.
517 More broadly, the E801 and D830 residues are conserved within the CoV family and the
518 D812 residue is conserved within betacoronaviruses (16, 17). The implication is that calcium
519 interactions are a conserved mechanism that serves to better position the FP for membrane
520 insertion. Different coronaviruses exhibit different requirements for calcium; MERS-CoV binds
521 to one calcium ion in its FP1 domain (25), thus, it is important to investigate the role of calcium
522 and FP interactions across the CoV family. Recent work using a FRET-assay has shown that
523 calcium interactions with the fusion peptide may drive the pre- to post-fusion conformational
524 changes in SARS CoV-2 spike (27). The authors of this study showed that alpha and beta
525 coronaviruses display a high sensitivity to calcium; the fusion activity of spike drops
526 precipitously as calcium levels rise or decrease past predicted late endosomal concentrations.
527 The conservation of calcium-binding residues in the FP of many coronaviruses suggests that the
528 CoV fusion mechanisms are essential for function and can serve as potential targets for broad-
529 spectrum antiviral drugs (38-40). Repurposing FDA-approved calcium channel blocking (CCB)
530 drugs to inhibit CoV entry, particularly for SARS-CoV-2, is one option worth exploring. Recent
531 studies have shown that the CCB felodipine is a potential candidate to inhibit SARS-CoV-2 entry
532 (41). CCBs can target conserved viral functions, providing a rapid solution to address new and
533 future SARS-CoV-2 variants. It will be important to identify the mechanisms of CCBs CoV
534 inhibition, as they may directly inhibit a viral target or indirectly inhibit viral entry by affecting
535 host cell processes. Interestingly, SARS-CoV-2 variants have arisen as part of Clade 20A that
536 contain a D839G or D839Y mutation (E821 equivalent in SARS-CoV-1), with this mutation

537 predicted to affect FP-Calcium interactions (42-44). To date, it is not known if there is any
538 selective advantage to the virus conferred by this mutation or whether the emergence of these
539 variants simply represents a founder effect. Future studies will continue to illustrate the role of
540 the spike FP in controlling both emerging and existing coronaviruses.

541

542 ## Materials and Methods

543

544 **Cells, plasmids, and reagents.** Human embryonic kidney 293 (HEK293T) and African green
545 monkey kidney epithelial (VeroE6) cells were obtained from the American Type Culture
546 Collection (ATCC, Manassas, VA). Both cell lines were grown in complete DMEM, composed of
547 Dulbecco's Modified Eagle medium (DMEM, CellGro), supplemented with 10% HyClone
548 FetalClone II (GE) and 10 mM HEPES (CellGro), and grown at 37°C with 5% CO_2. The plasmids
549 used for generating pseudoparticles were the pCMV-MLV gag-pol murine leukemia virus (MLV)
550 packaging construct, the pTG-Luc transfer vector encoding the luciferase reporter gene, and the
551 pCAGGS-VSVG plasmids. They were generously provided by Jean Dubuisson (Lille Pasteur
552 Institute, Lille, France) and co-transfected as previously described (24). The plasmid encoding
553 the C9-tagged SARS-CoV-1 spike protein (pcDNA3.1-C9-SARS-CoV-1 S) was provided by Dr.
554 Michael Farzan from the New England Primate Research Center. Recombinant L-1-tosylamide-
555 2-phenylethyl chloromethyl ketone (TPCK)-treated trypsin was obtained from Sigma. The
556 calcium chelators EGTA and BAPTA-AM (acetoxymethyl ester) were obtained from VWR and
557 Tocris, respectively. Both compounds were diluted in dimethyl sulfoxide (ThermoFisher) prior to
558 use.

559 **Site-directed mutagenesis.** Site-directed mutagenesis was performed on the SARS-CoV-1 spike
560 encoding plasmid, pcDNA3.1-SARS-CoV-1-S, via the QuikChange Lightning site-directed
561 mutagenesis kit (Aligent). PCRs and transformations were performed based on the
562 manufacturer's recommendations. The primers used to generate the SARS-CoV-1 S mutants can
563 be found in the supplementary information (**SI, Table S1**). Mutations were confirmed via Sanger
564 Sequencing at the Cornell University Life Sciences Core Laboratories Center.
565 **Cell Surface Biotinylation Assay.** HEK293T cells were seeded in poly-D-lysine coated 6-well
566 dishes. 24 hours later, cells were transfected with 1.5 ug of WT or mutant SARS-CoV-1 S plasmid
567 using polyethylenimine (PEI) (Thermo Fisher Scientific). Cells were transfected for 24 hours,
568 washed once with 1X DPBS, and then left untreated or treated with 1 mg/mL of TPCK-trypsin in
569 DPBS for 5 minutes at 37°C. Cell surface proteins were then biotinylated by incubating rinsed
570 cells in a biotin-containing buffer (250 ug/mL in PBS) for 20 minutes. The biotin buffer was then
571 replaced with a quenching solution (50mM glycine in DPBS) and incubated for 30 minutes. Cells
572 were then lysed in ice for 15 minutes using a lysis buffer (0.1% Triton in 1x TBS) with protease
573 inhibitors (cOmplete Protease Inhibitor Cocktail). Lysates were collected and spun at 13,000
574 rpm for 10 minutes to pellet insoluble material. The lysates were then incubated overnight at 4°
575 C with equilibrated steptavidin beads to retrieve the biotinylated spike proteins. The captured
576 spike proteins were eluted by boiling the beads in 1x LDS sample buffer in the presence of DTT
577 (NuPAGE) for 10 minutes. Proteins were resolved on 4-12% gradient Bis-Tris gels (NuPAGE) and
578 transferred to PVDF membranes. The SARS-CoV-1 S protein was detected using the SARS-CoV-1
579 S rabbit polyclonal primary antibody (NR-4569, BEI resources) and Alexa Fluor 488-labeled goat

580 anti-rabbit secondary antibody (Invitrogen). The resulting protein bands were visualized using a
581 Chemidoc system with Image Lab image capture software (BioRad).
582
583 **Cell-cell fusion assay.** VeroE6 cells were seeded onto glass slides in a 24-well chamber slides
584 (Millipore). After 24 hours, cells were transfected using Lipofectamine according to the
585 manufacturer instructions. Following 18 hours of transfection, cells were washed with 1X DPBS
586 and trysinized with 2mg/mL TPCK-trypsin for 5 minutes at 37°C to. Cells were then fixed with
587 4% paraformaldehyde (PFA) (ThermoFisher) for 15 minutes and washed three times with DPBS.
588 To permeabilize the cells, a 0.1% Triton X-100 in DPBS solution was added to each well and cells
589 were incubated for 5 minutes. After three washes with DPBS, the cells were blocked with 5%
590 normal goat serum for 30 minutes. Cells were again washed and then labeled with SARS-CoV-1
591 S rabbit polyclonal antibody (NR-4569, BEI resources), followed by labeling with Alexa Fluor
592 488-labeled goat anti-rabbit secondary antibody (Invitrogen). The cell nuclei were labeled with
593 a DAPI stain present in the mounting media (DAPI Fluoromount-G, Southern Biotech). Images
594 were acquired using an upright microscope (Echo Revolve) with a 10x objective. To quantify the
595 number of nuclei per syncytia, three randomly selected fields were acquired and spike-
596 expressing cells and syncytia were manually counted. The total number of syncytia we counted
597 and expressed as a percentage of the total fluorescent "particles" that were counted in the
598 image. The data was graphed and statistics were carried out using Microsoft Excel and
599 GraphPad Prism 7.
600 **SARS-CoV-1 pseudoparticle infectivity assay.** SARS-CoV-1 pseudoparticles were produced as
601 previously described (24, 25). Briefly, to generate pseudoparticles 3.5 x10^5 HEK293T cells were

602 seeded in 6-well plates. Pseudoparticles were prepared by transfecting HEK293T cells with 600
603 µg of their respective SARS WT or mutant S plasmids, 800 µg of pTG-Luc plasmid, and 600 µg of
604 pCMV-MLV gag-pol plasmid using polyethylenimine (PEI) as the transfection reagent. The cell
605 supernatant was harvested 48 hours post-transfection, centrifuged at 1200 rpm for 7 minutes
606 to separate the pseudoparticles from residual cellular debris, and filtered through a 0.45 µm
607 syringe filter. The pseudoparticles were stored at -80°C for one freeze-thaw cycle. To perform
608 the pseudoparticle infectivity assay, $5x10^5$ VeroE6 cells were seeded into 24-well plates and
609 infected with 200uL of the pseudoparticle suspension for 72 hrs at 37°C. Cells were lysed for 10
610 minutes at room temperature using the Luciferase cell lysis reagent (Promega). Luminescence
611 readings were performed using a Glomax 20/20 Luminometer system (Promega). Each
612 experiment contained three technical replicates and was repeated at least three times. Data
613 analysis was performed using GraphPad Prism 7.

614 For the calcium depletion studies, calcium was chelated from the extracellular and
615 intracellular environment using EGTA or BAPTA-AM, respectively. To deplete extracellular
616 calcium levels, VeroE6 cells were pre-treated with DMEM lacking calcium (DMEM- lacks L-
617 glutamine, sodium pyruvate, HEPES, and calcium; it contains 2% HyClone and 10 mM HEPES) for
618 1 hour at 37°C. After the DMEM- pretreatment, the VeroE6 cells were infected with 200 µL of
619 pseudoparticle suspension in the presence of 50 µM EGTA for 2 hours at 37°C. Following
620 infection, cells were supplemented with 300 µL of calcium-containing cDMEM.

621 To chelate the remaining intracellular calcium, VeroE6 cells were pretreated with 50 µM
622 BAPTA-AM in DMEM+ (DMEM without L-glutamine, sodium pyruvate, HEPES; 2% HyClone; 10
623 mM HEPES; Gibco) in the same conditions as described above. Cells were then infected using

624 200 µL of the pseudoparticle suspension in the presence of 50 µM BAPTA-AM for 2 hours and
625 supplemented with cDMEM post-infection. Because BAPTA-AM was dissolved in DMSO, VeroE6
626 cells were pretreated with the equivalent percentage of DMSO used in the BAPTA-AM treated
627 cells. This served as an important control for the effects of DMSO alone on our infectivity assay.
628 Analysis of pseudoparticle infectivity under calcium depletion conditions was performed as
629 described above. To confirm the presence of the S protein in the pseudoparticles, 1.5 mL of the
630 harvested pseudoparticles were spun down using an ultracentrifuge in a TLA-55 rotor
631 (Beckman-Coulter) at 42,000 × *g* for 2 hours at 4°C. The supernatant was aspirated and the S
632 protein-containing pellet was resuspended and boiled in 1x LDS sample buffer in the presence
633 of DTT for 10 minutes. The samples were resolved and immunoblotted for the spike protein as
634 described above.
635
636 **Modeling of the SARS-CoV-1 fusion peptide.** The structural model of the SARS-CoV-1 S protein
637 fusion peptide is based on the SARS-CoV-1 S prefusion structure from the Protein Data Bank,
638 PDB 5XLR. The sequence of the SARS-CoV-1 S protein (GenBank accession no. AAT74874.1) was
639 aligned to the PDB 5XLR SARS-CoV-1 structure sequence using Geneious software (**v.2020.1.1**).
640 Structural models of the SARS-CoV-1 S monomer were generated using the Modeller
641 comparative modeling tool (**v.9.23**) within the Chimera software (v.1.13; University of
642 California). Images were created using Adobe Illustrator CC (**v.24.03**).
643
644 **Molecular dynamics (MD) simulations of the SARS-CoV-1 FP in water.** For all the atomistic MD
645 simulations, the SARS-CoV-1 FP segment was capped with neutral N- and C-termini (ACE and

646 CT3, respectively, in the CHARMM force-field nomenclature). Protonation states of all the
647 titratable residues were predicted at pH 7 using Propka 3.1 software (45).

648 For the simulations in water, one copy of the peptide (wild-type or a mutant) was
649 embedded in a rectangular solution box and ionized using VMD tools ("Add Solvation Box" and
650 "Add Ions", respectively) (46). The box of dimensions ~90 Å x 80 Å x 82 Å included a Na^+Cl^- ionic
651 solution as well as 2 Calcium ions, and ~18000 water molecules. The total number of atoms in
652 the system was ~54,540.

653 The system was equilibrated with NAMD version 2.13 (47) following a multi-step protocol
654 during which the backbone atoms of the SARS-CoV-1 FP as well as Calcium ions in the solution
655 were first harmonically constrained and subsequently gradually released in four steps (totaling
656 ~3ns), changing the restrain force constants k_F from 1, to 0.5, to 0.1 kcal/ (mol $Å^2$), and 0 kcal/
657 (mol $Å^2$). These simulations implemented all option for rigidbonds, 1fs (for k_F 1, 0.5, and 0.1
658 kcal/ (mol $Å^2$)) or 2fs (for k_F of 0) integration time-step, PME for electrostatics interactions (48),
659 and were carried out in NPT ensemble under isotropic pressure coupling conditions, at a
660 temperature of 310 K. The Nose-Hoover Langevin piston algorithm (49) was used to control the
661 target P = 1 atm pressure with the "LangevinPistonPeriod" set to 200 fs and
662 "LangevinPistonDecay" set to 50 fs. The van der Waals interactions were calculated applying a
663 cutoff distance of 12 Å and switching the potential from 10 Å.

664 After this initial equilibration phase, the velocities of all atoms in the system were reset and
665 ensemble MD runs were initiated with OpenMM version 7.4 (50) during which the system was
666 simulated in 18 independent replicates, each for 640ns (i.e., cumulative time of ~11.5 µs for
667 each FP construct). These runs implemented PME for electrostatic interactions and were

668 performed at 310K temperature under NVT ensemble. In addition, 4fs time-step was used, with
669 hydrogen mass repartitioning and with "friction" parameter set to 1.0/picosecond. Additional
670 parameters for these runs included: "EwaldErrorTolerance" 0.0005, "rigidwater" True, and
671 "ConstraintTolerance" 0.000001. The van der Waals interactions were calculated applying a
672 cutoff distance of 12 Å and switching the potential from 10 Å.
673
674 **MD simulations of SARS-CoV-1 FP interactions with lipid membranes.** Interactions of selected
675 two models of the Calcium-bound WT SARS-CoV-1 FP with lipid membranes were investigated
676 with atomistic MD simulations. These runs were initiated by placing each of the models in the
677 proximity of a bilayer composed of 3:1:1 POPC/POPG/Cholesterol that had been pre-
678 equilibrated for 25ns as described previously (20).
679 After the FP-membrane complexes were embedded in a solution box (containing 150 mM
680 Na^+Cl^- salt concentration), each system was equilibrated with NAMD version 2.13 following the
681 same multi-step protocol described above during which the backbone atoms of the FP as well
682 as the Calcium ions were first harmonically constrained and subsequently gradually released in
683 four steps. After this phase, the velocities of all atoms of the system were reset, and ensemble
684 MD runs were initiated with OpenMM version 7.4. Each system was simulated in 18
685 independent replicates, each ran for ~ 1 µs (i.e., cumulative time of ~18 µs for each FP-
686 membrane complex). These runs implemented PME for electrostatic interactions and were
687 performed at 298K temperature under NPT ensemble using semi-isotropic pressure coupling,
688 with 4fs time-steps, using hydrogen mass repartitioning and with "friction" parameter set to
689 1.0/picosecond. Additional parameters for these runs included: "EwaldErrorTolerance" 0.0005,

690 “rigidwater” True, and “ConstraintTolerance” 0.000001. The van der Waals interactions were
691 calculated applying a cutoff distance of 12 Å and switching the potential from 10 Å. For all
692 simulations we used the latest CHARMM36 force-field for proteins and lipids (51), as well as the
693 recently revised CHARMM36 force-field for ions which includes non-bonded fix (NBFIX)
694 parameters for Na^+ and Calcium ions (52).
695

696 **Acknowledgements**

697 This work was supported by The National Institute of Health research grant R01AI35270,
698 National Science Foundation RAPID grant 2027070 and Fast Grant from the Mercatus Center at
699 George Mason University. TT is supported by the National Science Foundation Graduate
700 Research Fellowship Program under Grant No. DGE-1650441 and the Samuel C. Fleming Family
701 Graduate Fellowship. H.W. and G.K. gratefully acknowledge support from the 1923 Fund, and
702 the access to computational resources awarded through the COVID-19 High Performance
703 Computing Consortium at the Center for Computational Innovations (CCI) at the Rensselaer
704 Polytechnic Institute and at the Oak Ridge Leadership Computing Facility, which is a DOE Office
705 of Science User Facility supported under Contract DE-AC05-00OR22725. We would like to thank
706 members of the Daniel, Whittaker, and Abbott groups as well as the Weinstein group at Weill
707 Cornell for helpful discussions.
708

709 **Author Contributions**

710 Conceived and designed the experiments: MKB GK MRS HW GRW SD. Performed the
711 experiments: MKB JDC GK MRS TT. Analyzed the data: MKB JDC GK MRS TT HW GRW SD.
712 Wrote and edited the paper: JDC MKB GK MRS TT HW GRW SD. Acquired funding: GRW SD.
713

714

715

716 **References**

717

718 1. Lai MM, Cavanagh D. The molecular biology of coronaviruses. Adv Virus Res. 1997;48:1-
719 100.
720 2. Masters PS. The molecular biology of coronaviruses. Adv Virus Res. 2006;66:193-292.
721 3. Cherry JD, Krogstad P. SARS: the first pandemic of the 21st century. Pediatr Res.
722 2004;56(1):1-5.
723 4. de Groot RJ, Baker SC, Baric RS, Brown CS, Drosten C, Enjuanes L, et al. Middle East
724 respiratory syndrome coronavirus (MERS-CoV): announcement of the Coronavirus Study Group.
725 J Virol. 2013;87(14):7790-2.
726 5. Wu F, Zhao S, Yu B, Chen YM, Wang W, Song ZG, et al. A new coronavirus associated
727 with human respiratory disease in China. Nature. 2020;579(7798):265-9.
728 6. Zhou P, Yang XL, Wang XG, Hu B, Zhang L, Zhang W, et al. A pneumonia outbreak
729 associated with a new coronavirus of probable bat origin. Nature. 2020;579(7798):270-3.
730 7. de Wit E, van Doremalen N, Falzarano D, Munster VJ. SARS and MERS: recent insights
731 into emerging coronaviruses. Nat Rev Microbiol. 2016;14(8):523-34.
732 8. Shulla A, Heald-Sargent T, Subramanya G, Zhao J, Perlman S, Gallagher T. A
733 transmembrane serine protease is linked to the severe acute respiratory syndrome coronavirus
734 receptor and activates virus entry. J Virol. 2011;85(2):873-82.
735 9. Millet JK, Whittaker GR. Host cell proteases: Critical determinants of coronavirus
736 tropism and pathogenesis. Virus Res. 2015;202:120-34.
737 10. Stevens CS, Oguntuyo KY, Lee B. Proteases and variants: context matters for SARS-CoV-2
738 entry assays. Curr Opin Virol. 2021;50:49-58.
739 11. Matsuyama S, Ujike M, Morikawa S, Tashiro M, Taguchi F. Protease-mediated
740 enhancement of severe acute respiratory syndrome coronavirus infection. Proc Natl Acad Sci U
741 S A. 2005;102(35):12543-7.
742 12. Tang T, Bidon M, Jaimes JA, Whittaker GR, Daniel S. Coronavirus membrane fusion
743 mechanism offers a potential target for antiviral development. Antiviral Res. 2020;178:104792.
744 13. Belouzard S, Chu VC, Whittaker GR. Activation of the SARS coronavirus spike protein via
745 sequential proteolytic cleavage at two distinct sites. Proc Natl Acad Sci U S A.
746 2009;106(14):5871-6.
747 14. Bosch BJ, Bartelink W, Rottier PJ. Cathepsin L functionally cleaves the severe acute
748 respiratory syndrome coronavirus class I fusion protein upstream of rather than adjacent to the
749 fusion peptide. J Virol. 2008;82(17):8887-90.
750 15. Jaimes JA, Andre NM, Chappie JS, Millet JK, Whittaker GR. Phylogenetic Analysis and
751 Structural Modeling of SARS-CoV-2 Spike Protein Reveals an Evolutionary Distinct and
752 Proteolytically Sensitive Activation Loop. J Mol Biol. 2020;432(10):3309-25.

753 16. Madu IG, Roth SL, Belouzard S, Whittaker GR. Characterization of a highly conserved
754 domain within the severe acute respiratory syndrome coronavirus spike protein S2 domain with
755 characteristics of a viral fusion peptide. J Virol. 2009;83(15):7411-21.
756 17. Lai AL, Millet JK, Daniel S, Freed JH, Whittaker GR. The SARS-CoV Fusion Peptide Forms
757 an Extended Bipartite Fusion Platform that Perturbs Membrane Order in a Calcium-Dependent
758 Manner. J Mol Biol. 2017;429(24):3875-92.
759 18. Madu IG, Belouzard S, Whittaker GR. SARS-coronavirus spike S2 domain flanked by
760 cysteine residues C822 and C833 is important for activation of membrane fusion. Virology.
761 2009;393(2):265-71.
762 19. Lai AL, Freed JH. SARS-CoV-2 Fusion Peptide has a Greater Membrane Perturbating
763 Effect than SARS-CoV with Highly Specific Dependence on Ca(2). J Mol Biol.
764 2021;433(10):166946.
765 20. Khelashvili G, Plante A, Doktorova M, Weinstein H. Ca(2+)-dependent mechanism of
766 membrane insertion and destabilization by the SARS-CoV-2 fusion peptide. Biophys J.
767 2021;120(6):1105-19.
768 21. Lai AL, Freed JH. Negatively charged residues in the membrane ordering activity of SARS-
769 CoV-1 and -2 fusion peptides. Biophys J. 2022;121(2):207-27.
770 22. Gui M, Song W, Zhou H, Xu J, Chen S, Xiang Y, et al. Cryo-electron microscopy structures
771 of the SARS-CoV spike glycoprotein reveal a prerequisite conformational state for receptor
772 binding. Cell Res. 2017;27(1):119-29.
773 23. Wang H, Yang P, Liu K, Guo F, Zhang Y, Zhang G, et al. SARS coronavirus entry into host
774 cells through a novel clathrin- and caveolae-independent endocytic pathway. Cell Res.
775 2008;18(2):290-301.
776 24. Millet JK, Tang T, Nathan L, Jaimes JA, Hsu HL, Daniel S, et al. Production of Pseudotyped
777 Particles to Study Highly Pathogenic Coronaviruses in a Biosafety Level 2 Setting. J Vis Exp.
778 2019(145).
779 25. Straus MR, Tang T, Lai AL, Flegel A, Bidon M, Freed JH, et al. Ca(2+) Ions Promote Fusion
780 of Middle East Respiratory Syndrome Coronavirus with Host Cells and Increase Infectivity. J
781 Virol. 2020;94(13).
782 26. Tang T, Jaimes JA, Bidon MK, Straus MR, Daniel S, Whittaker GR. Proteolytic Activation
783 of SARS-CoV-2 Spike at the S1/S2 Boundary: Potential Role of Proteases beyond Furin. ACS
784 Infect Dis. 2021;7(2):264-72.
785 27. Singh P, Mukherji S, Basak S, Hoffmann M, Das DK. Dynamic Ca(2+) sensitivity stimulates
786 the evolved SARS-CoV-2 spike strain-mediated membrane fusion for enhanced entry. Cell Rep.
787 2022;39(3):110694.
788 28. Sultan F, Ahuja K, Motiani RK. Potential of targeting host cell calcium dynamics to curtail
789 SARS-CoV-2 infection and COVID-19 pathogenesis. Cell Calcium. 2022;106:102637.
790 29. Dakal TC. SARS-CoV-2 attachment to host cells is possibly mediated via RGD-integrin
791 interaction in a calcium-dependent manner and suggests pulmonary EDTA chelation therapy as
792 a novel treatment for COVID 19. Immunobiology. 2021;226(1):152021.
793 30. Lambert DW, Clarke NE, Hooper NM, Turner AJ. Calmodulin interacts with angiotensin-
794 converting enzyme-2 (ACE2) and inhibits shedding of its ectodomain. FEBS Lett.
795 2008;582(2):385-90.

796 31. Lai ZW, Lew RA, Yarski MA, Mu FT, Andrews RK, Smith AI. The identification of a
797 calmodulin-binding domain within the cytoplasmic tail of angiotensin-converting enzyme-2.
798 Endocrinology. 2009;150(5):2376-81.
799 32. Garcia-Escobar A, Vera-Vera S, Jurado-Roman A, Jimenez-Valero S, Galeote G, Moreno
800 R. Calcium Signaling Pathway Is Involved in the Shedding of ACE2 Catalytic Ectodomain: New
801 Insights for Clinical and Therapeutic Applications of ACE2 for COVID-19. Biomolecules.
802 2022;12(1).
803 33. Lai AL, Freed JH. SARS-CoV-2 Fusion Peptide has a Greater Membrane Perturbating
804 Effect than SARS-CoV with Highly Specific Dependence on Ca2+. Journal of Molecular Biology.
805 2021;433(10):166946.
806 34. Khelashvili G, Plante A, Doktorova M, Weinstein H. Ca^{2+}-dependent mechanism of
807 membrane insertion and destabilization by the SARS-CoV-2 fusion peptide. Biophysical Journal.
808 2021;120(6):1105-19.
809 35. Koppisetti RK, Fulcher YG, Van Doren SR. Fusion Peptide of SARS-CoV-2 Spike
810 Rearranges into a Wedge Inserted in Bilayered Micelles. J Am Chem Soc. 2021;143(33):13205-
811 11.
812 36. Schaefer SL, Jung H, Hummer G. Binding of SARS-CoV-2 Fusion Peptide to Host
813 Endosome and Plasma Membrane. J Phys Chem B. 2021;125(28):7732-41.
814 37. Cai Y, Zhang J, Xiao T, Peng H, Sterling SM, Walsh RM, Jr., et al. Distinct conformational
815 states of SARS-CoV-2 spike protein. Science. 2020;369(6511):1586-92.
816 38. Straus MR, Bidon MK, Tang T, Jaimes JA, Whittaker GR, Daniel S. Inhibitors of L-Type
817 Calcium Channels Show Therapeutic Potential for Treating SARS-CoV-2 Infections by Preventing
818 Virus Entry and Spread. ACS Infect Dis. 2021;7(10):2807-15.
819 39. Crespi B, Alcock J. Conflicts over calcium and the treatment of COVID-19. Evol Med
820 Public Health. 2021;9(1):149-56.
821 40. Danta CC. Calcium Channel Blockers: A Possible Potential Therapeutic Strategy for the
822 Treatment of Alzheimer's Dementia Patients with SARS-CoV-2 Infection. ACS Chem Neurosci.
823 2020;11(15):2145-8.
824 41. Straus MR, Bidon M, Tang T, Whittaker GR, Daniel S. FDA approved calcium channel
825 blockers inhibit SARS-CoV-2 infectivity in epithelial lung cells. bioRxiv. 2020:2020.07.21.214577.
826 42. Korber B, Fischer WM, Gnanakaran S, Yoon H, Theiler J, Abfalterer W, et al. Tracking
827 Changes in SARS-CoV-2 Spike: Evidence that D614G Increases Infectivity of the COVID-19 Virus.
828 Cell. 2020;182(4):812-27 e19.
829 43. Li Q, Wu J, Nie J, Zhang L, Hao H, Liu S, et al. The Impact of Mutations in SARS-CoV-2
830 Spike on Viral Infectivity and Antigenicity. Cell. 2020;182(5):1284-94 e9.
831 44. Olsson MH, Sondergaard CR, Rostkowski M, Jensen JH. PROPKA3: Consistent Treatment
832 of Internal and Surface Residues in Empirical pKa Predictions. J Chem Theory Comput.
833 2011;7(2):525-37.
834 45. Olsson MHM, Søndergaard CR, Rostkowski M, Jensen JH. PROPKA3: Consistent
835 Treatment of Internal and Surface Residues in Empirical pKa Predictions. Journal of Chemical
836 Theory and Computation. 2011;7(2):525-37.
837 46. Humphrey W, Dalke A, Schulten K. VMD: visual molecular dynamics. J Mol Graph.
838 1996;14(1):33-8, 27-8.

839 47. Phillips JC, Braun R, Wang W, Gumbart J, Tajkhorshid E, Villa E, et al. Scalable molecular
840 dynamics with NAMD. J Comput Chem. 2005;26(16):1781-802.
841 48. Essmann U, Perera L, Berkowitz ML, Darden T, Lee H, Pedersen LG. A smooth particle
842 mesh Ewald method. The Journal of Chemical Physics. 1995;103(19):8577-93.
843 49. Evans DJ, Holian BL. The Nose–Hoover thermostat. The Journal of Chemical Physics.
844 1985;83(8):4069-74.
845 50. Eastman P, Swails J, Chodera JD, McGibbon RT, Zhao Y, Beauchamp KA, et al. OpenMM
846 7: Rapid development of high performance algorithms for molecular dynamics. PLoS Comput
847 Biol. 2017;13(7):e1005659.
848 51. Huang J, Rauscher S, Nawrocki G, Ran T, Feig M, de Groot BL, et al. CHARMM36m: an
849 improved force field for folded and intrinsically disordered proteins. Nature Methods.
850 2017;14(1):71-3.
851 52. Venable RM, Luo Y, Gawrisch K, Roux B, Pastor RW. Simulations of anionic lipid
852 membranes: development of interaction-specific ion parameters and validation using NMR
853 data. J Phys Chem B. 2013;117(35):10183-92.
854